

# Spatially Resolved Elastic Modulus of Magnesium Silicate Hydrate: A Cementitious Material

Arif Syed, Trinh Thao My Nguyen, and Erika La Plante\*



Cite This: *ACS Appl. Eng. Mater.* 2024, 2, 1047–1055

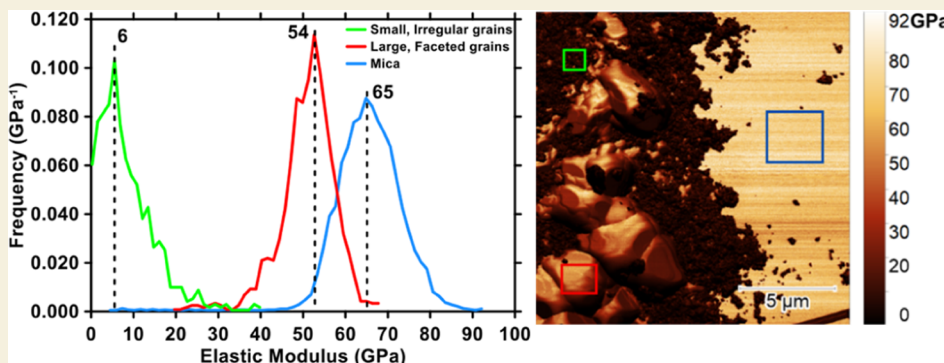


Read Online

ACCESS |

Metrics & More

Article Recommendations



**ABSTRACT:** Magnesium-based cement such as magnesium silicate hydrate (M–S–H) has drawn interest as a substitute for ordinary Portland cement. The precise determination of M–S–H's elastic modulus is essential in assessing the mechanical performance of M–S–H-based concrete. Atomic force microscopy (AFM) allows for spatially resolved quantification of nanomechanical characteristics of materials, including thin overgrowths on substrates. In this study, elastic modulus maps of M–S–H grown on single crystal mica surfaces were obtained using amplitude modulation–frequency modulation AFM. The effects of the Mg-to-Si molar ratio and morphology on the elastic modulus of M–S–H films were investigated. AFM reveals elastic moduli ranging from 5 to 15 and 40 to 64 GPa, depending on the growth reaction time and morphology. A comparison with calcium silicate hydrate found in traditional cement reveals insights into the influence of silicate polymerization on the material's stiffness. These findings demonstrate the effectiveness of AFM in quantitatively describing the mechanical characteristics of cementitious phases and suggest that M–S–H cement has the potential for use in a variety of construction applications.

**KEYWORDS:** mechanical properties, atomic force microscopy, amplitude modulation-frequency modulation, alternative cement

## 1. INTRODUCTION

Magnesium silicate hydrate (M–S–H) is a potential alternative to calcium silicate hydrate (C–S–H) composing ordinary Portland cement (OPC) traditionally used in construction.<sup>1–4</sup> By substituting for C–S–H, the strain on calcium resources is reduced while taking advantage of the plentiful magnesium supply, e.g., in rocks rich in magnesium silicates.<sup>5–8</sup> However, the use of M–S–H in construction applications is currently limited, in part because of a lack of knowledge regarding its cementitious qualities, particularly its mechanical properties, durability, and long-term performance.

The elastic modulus of cementitious materials describes their capacity to endure elastic deformation under applied stresses. It is crucial for evaluating the strength, resilience, and overall performance of concrete. For instance, in applications where stiffness and load-bearing capability are desired, such as in high-rise buildings or bridges, a rigid material that can effectively resist deformation and convey stress is desired.<sup>9</sup> On the contrary, a low elastic modulus is characteristic of a flexible

material that can withstand loads and motions and is preferred for applications requiring compatibility with thermal expansion or fracture resistance, such as pavements or structures exposed to large temperature fluctuations.<sup>10,11</sup> Therefore, the design, durability, and serviceability of concrete structures depend on an understanding of the elastic modulus.

The elastic moduli of cement—typically measured for a paste, mortar, or concrete, instead of a specific hydrate in the binder such as C–S–H—have been studied using non-destructive techniques,<sup>12</sup> nanoindentations,<sup>13</sup> finite element analysis,<sup>14</sup> and molecular dynamics simulations.<sup>15</sup> It has been

Received: January 31, 2024

Revised: March 26, 2024

Accepted: March 26, 2024

Published: April 8, 2024



shown using nanoindentation that elastic modulus increases with decreasing porosity.<sup>13</sup> Nondestructive testing of concrete is increasingly acknowledged for evaluating strength, durability, and structural properties.<sup>12</sup> In addition, finite element analysis reveals stress accumulation and restoration patterns,<sup>14</sup> whereas molecular dynamics simulations prove effective in predicting the elastic properties of hydrated cement paste constituents.<sup>15</sup> The composition, water-to-cement ratio, curing conditions, and aggregate qualities affect the elastic modulus of concrete.<sup>16,17</sup> For instance, it has been shown that both extensive curing and the addition of supplementary cementitious materials to OPC concrete marginally decrease workability but significantly improve mechanical properties.<sup>16,18</sup> However, to the best of our knowledge, the mechanical properties, including the elastic modulus, of M–S–H remain largely unexplored.

In this study, we characterize the elastic modulus of M–S–H grown on single-crystal mica using amplitude modulation–frequency modulation atomic force microscopy (AM–FM AFM). To ascertain the nature and distribution of associated phases (if any), M–S–H was also synthesized as a bulk powder and characterized using a suite of tools including X-ray diffraction (XRD), thermogravimetric analysis (TGA), Fourier-transform infrared spectroscopy (FTIR), and scanning electron microscopy with energy-dispersive spectroscopy (SEM-EDS). This study demonstrates the unique capability of AFM in spatially resolving the mechanical properties of diverse materials, such as cement, at the nanoscale. The elastic modulus of M–S–H, measured for the first time in this study, is compared with that of C–S–H. Investigating M–S–H’s mechanical properties at high spatial and temporal resolutions provides insights into the fundamental origins underlying its cementitious characteristics. Moreover, insights gained from this study can be extrapolated to lesser-explored magnesium-based cement. Our results support the viability of M–S–H as a binding material in construction and a potential alternative to conventional cement.

## 2. MATERIALS AND METHODS

### 2.1. Sample Preparation

The samples were prepared by mixing stock solutions of magnesium nitrate hexahydrate ( $\text{Mg}(\text{NO}_3)_2 \cdot 6\text{H}_2\text{O}$ , 95% purity), sodium metasilicate pentahydrate ( $\text{Na}_2\text{SiO}_3 \cdot 5\text{H}_2\text{O}$ , 99% purity), and ultrapure water ( $>18.2\text{ M}\Omega\text{-cm}$ ) in a polypropylene centrifuge tube, following a previously published procedure.<sup>4</sup> Bulk (powder) samples were prepared by adding 6 mL of each stock solution in a polypropylene centrifuge tube for a target final concentration of  $[\text{Mg}] = [\text{Si}] = 100\text{ mM}$  and a final volume of 12 mL. A multiparameter benchtop meter (ThermoFisher Scientific Orion VersaStar Pro) calibrated over  $4 < \text{pH} < 12$  was used to measure the pH values of the growth solution immediately following mixing of the stock solutions (Table 1). Then, the growth solution was set aside at ambient temperature ( $25 \pm 2^\circ\text{C}$ ) for 48 h to allow precipitates to form and settle at the bottom of the tube. At the end of the reaction period, the residual growth solution was decanted and 1 mL of ethanol was introduced into the tube to minimize further reaction. Subsequently, the tube was centrifuged twice at 2500 rpm for 20 min to separate the precipitates from the excess solution. The supernatant was decanted, and the wet precipitates were dried under vacuum conditions at  $25^\circ\text{C}$ . Once dried, the precipitates (wrapped in paper) were finely ground into a powder using a heavy metal chisel. A similar procedure was followed to prepare brucite ( $\text{Mg}(\text{OH})_2$ ) powder using stock solutions of  $\text{NaOH}$  and  $\text{Mg}(\text{NO}_3)_2 \cdot 6\text{H}_2\text{O}$ .

To prepare M–S–H samples for elastic modulus measurements, 1 mL of each stock solution was mixed in a centrifuge tube to achieve

**Table 1. Experimental Conditions for Bulk/Powder M–S–H Samples, Showing Mg/Si Ratios, Mg and Si Concentrations, Calculated pH, pH Measured Immediately after Mixing of the Stock Solutions (“Initial”), pH Measured after Reaction (“Final”), Reaction Time, and Reaction Temperature<sup>a</sup>**

$[\text{Mg}]/[\text{Si}]$	[Mg] (mM)	[Si] (mM)	pH (calc.)	pH (initial)	pH (final)	time (h)	temp. ( $^\circ\text{C}$ )
1	100	100	11.61	10.59	9.62	48.0	24.1
1	500	500	11.91	10.19	9.92	48.0	25.3
1	100	100	11.61	10.26	9.74	48.0	24.2

<sup>a</sup>pH is calculated using PHREEQC<sup>39</sup> with the Cemdata18<sup>40</sup> database.

Mg-to-Si molar ratios of 0.5, 1, 1.5, and 2 (Table 2). The reference material and substrate is a single-crystal disc of muscovite mica (001),

**Table 2. Experimental Conditions for M–S–H Grown on Mica, Showing Mg/Si Ratios, Mg and Si Concentrations, Calculated pH, pH Measured Immediately after Mixing of the Stock Solutions (“Initial”), pH Measured after Reaction (“Final”), Reaction Time, and Reaction Temperature<sup>a</sup>**

$[\text{Mg}]/[\text{Si}]$	[Mg] (mM)	[Si] (mM)	pH (calc.)	pH (initial)	pH (final)	time (h)	temp. ( $^\circ\text{C}$ )
0.5	50	100	12.58	10.19	9.85	48.3	23.1
1.0	100	100	11.70	10.29	9.88	0.7	22.3
1.0	100	100	11.67	10.16	9.77	0.7	23.1
1.0	100	100	11.68	10.40	9.62	24.6	22.9
1.0	100	100	11.68	10.40	9.58	24.6	22.9
1.0	100	100	11.70	10.29	9.46	94.1	22.3
1.0	100	100	11.67	10.41	9.46	112.5	23.1
1.0	100	100	11.64	10.59	9.62	48.1	24.1
1.5	150	100	10.98	9.56	9.10	0.7	23.1
1.5	150	100	10.97	9.72	9.46	48.1	23.3
2.0	200	100	10.74	9.49	9.04	0.7	24.0
2.0	200	100	10.76	9.73	8.75	48.1	23.3

<sup>a</sup>pH is calculated using PHREEQC<sup>39</sup> with the Cemdata18<sup>40</sup> database. For a growth solution with a  $[\text{Mg}]/[\text{Si}]$  ratio of 1 and a pH of 11.70, the saturation indices with respect to  $\text{M}_{0.5}\text{SH}$  and  $\text{M}_{1.5}\text{SH}$  are 9.61 and 8.57, respectively.

grade V1 (Ted Pella), 10 mm in diameter and 0.2 mm in thickness. The mica disc was cleaved to ensure a clean surface, and any debris was removed by brief exposure to ultrahigh purity (UHP) nitrogen gas. The cleaved mica disc is then placed immediately in a centrifuge tube containing 2 mL of growth solution. To allow M–S–H to precipitate on the mica surface, the tube was sealed and then stored at ambient temperature ( $25 \pm 2^\circ\text{C}$ ) for up to 112 h (Table 2). The pH values of the growth solutions were measured upon mixing the stock solutions and at the end of the reaction. Following the pH measurements, the mica disc was carefully removed from the centrifuge tube. Excess liquid was removed from the edge of the mica disc by using a Kimwipe, and the disc was then briefly exposed to UHP nitrogen to ensure the removal of any remaining liquid. The samples were then stored in a lidded polyethylene container under ambient conditions until they were ready to be characterized by AFM. The elastic modulus of mica was measured using a Hysitron Ubi1 Nano-Indenter with a diamond tip.

### 2.2. Characterization of M–S–H Powder

Geochemical modeling of the growth solution shows supersaturation with respect to M–S–H and brucite ( $\text{Mg}(\text{OH})_2$ ) and undersaturation with respect to amorphous silica ( $\text{SiO}_{2(\text{am})}$ ).<sup>4</sup> To confirm the nature and abundance of phases that coprecipitate with M–S–H (if any), the powder samples were characterized using XRD, FTIR, TGA, and SEM-EDS. To characterize the crystallographic structure of

the powder precipitates, a D8 Advance X-ray diffractometer (Bruker) with a Cu  $K\alpha$  source ( $\lambda = 1.5418 \text{ \AA}$ ) was used. The data were collected at  $2\theta$  ranging from 5 to  $80^\circ$  with an increment of  $0.01^\circ$  and  $0.5^\circ/\text{min}$  scan rate at a voltage and current of 40 kV and 40 mA, respectively. A Nicolet iSSO FTIR spectrometer (Thermo Fisher Scientific) was used to perform infrared absorbance measurements. An attenuated total reflectance (ATR) attachment and a deuterated triglycine sulfate (DTGS) KBr detector were fitted to the apparatus. The infrared spectra were obtained with the atmospheric suppression option enabled over a wavenumber range of 525 to  $4000 \text{ cm}^{-1}$ , and 32 scans were collected. TGA was performed using an SDT-Q600 simultaneous TGA/differential scanning calorimeter (DSC) (TA Instruments). Data were collected over a temperature range of 20 to  $1050^\circ\text{C}$  with an increment of  $15^\circ\text{C}/\text{min}$  and a nitrogen gas flow rate of 20 mL/min. SEM-EDS was performed using a S-3000N variable pressure SEM (Hitachi) with a tungsten electron source. Before imaging, the samples were coated with lead in the presence of argon gas by using a CrC-100 sputtering system. An accelerating voltage of 20 kV, magnification of 200 $\times$ , beam current of 62 nA, and working distance of 15 mm were used.

### 2.3. Measurement of Elastic Modulus at the Nanoscale

Amplitude modulation–frequency modulation (AM–FM) AFM was used to quantify the elastic modulus of the M–S–H overgrowths. In AM–FM, amplitude modulation (AM) enables the characterization of surface topography, while frequency modulation (FM) provides nanomechanical characteristics of the sample surface, including the elastic modulus.<sup>19,20</sup> A high-amplitude drive is applied to the primary resonance frequency of the cantilever, while a low-amplitude drive is applied to its second resonance frequency. Shifts in the second resonance frequency are related to the sample's elastic modulus.<sup>21</sup> The analysis presented herein uses a reference material with a known elastic modulus,  $E$  (herein, single-crystal mica with  $E = 64 \pm 2 \text{ GPa}$ ), to determine the unknown elastic modulus of the sample (herein, M–S–H). The known elastic modulus of the reference material is used to obtain the best-fit parameters that describe tip–sample interactions, including tip–sample Hertzian contact mode (e.g., Hertz Punch, Hertz Cone, Hertz Sphere) and tip geometry (e.g., tip radius and half-cone angle), enabling quantitative determination of the unknown elastic modulus. Therefore, a priori knowledge of specific tip–sample interactions is not required. AFM data were collected using a silicon probe having a rectangular cantilever with a 70 nm-thick gold coating on the detector side, force constant of 3 N/m, nominal resonance frequency of 75 kHz, length of 225  $\mu\text{m}$ , width of 28  $\mu\text{m}$ , and thickness of 3  $\mu\text{m}$ .

## 3. RESULTS AND DISCUSSION

### 3.1. Analysis of Associated Phases

The conditions for the bulk (powder) synthesis performed in this study are shown in Table 1. The chemical composition of M–S–H is influenced by several variables, including the reaction duration, chemical composition of precursors, temperature, Mg/Si ratio, and water activity.<sup>22–24</sup> Furthermore, previous studies characterizing synthetic M–S–H reveal the presence of associated phases such as brucite and amorphous silica.<sup>25,26</sup> XRD, TGA, and FTIR show that the precipitates that formed under our experimental conditions are primarily M–S–H. Specifically, XRD data for M–S–H reveal characteristic broad humps at  $2\theta = 20.1, 26.7, 35.0$ , and  $59.9^\circ$  (Figure 1).<sup>25–30</sup> FTIR analysis also shows that brucite is not present in significant quantities (estimated to be  $<3\%$  by mass of the precipitates, based on the typical instrumental resolution of techniques employed herein) (Figure 2).<sup>26,30,31</sup> Silicate tetrahedral polymerization in M–S–H ( $\sim 600\text{--}1400 \text{ cm}^{-1}$ ) can be characterized from the relative amounts of  $Q^1$  (one oxygen shared between two silicon atoms, forming chains),  $Q^2$  (two shared oxygens, forming double chains), and  $Q^3$  (three

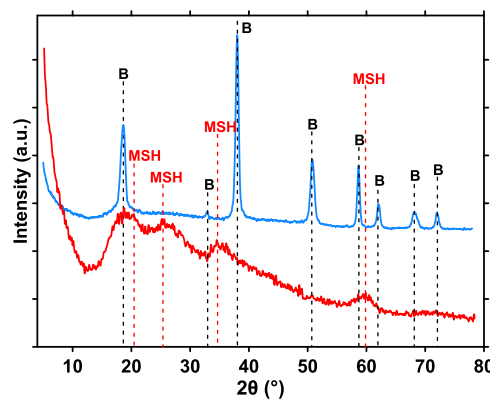


**Figure 1.** X-ray diffraction pattern of the precipitates grown from a solution containing either (red)  $[\text{Mg}] = [\text{Si}] = 100 \text{ mM}$  or (blue)  $[\text{Mg}] = [\text{OH}] = 100 \text{ mM}$  reacted for 48 h at  $25 \pm 2^\circ\text{C}$ , matching that of either M–S–H<sup>37</sup> or brucite.<sup>41,42</sup>

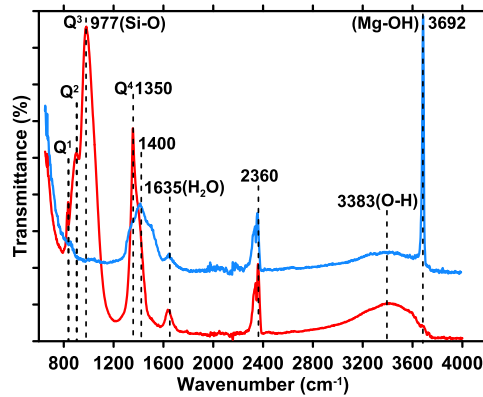


**Figure 2.** Infrared absorbance spectra of the precipitates grown from a solution containing either (red)  $[\text{Mg}] = [\text{Si}] = 100 \text{ mM}$  or (blue)  $[\text{Mg}] = [\text{OH}] = 100 \text{ mM}$  reacted for 48 h at  $25 \pm 2^\circ\text{C}$ . The peak at  $2360 \text{ cm}^{-1}$  is associated with atmospheric  $\text{CO}_2$ .

shared oxygens, forming sheets) species,<sup>32–34</sup> with  $Q^3$  representing M–S–H sheets and  $Q^2$  representing defects within these sheets.<sup>4</sup> Distinct peaks between  $\sim 600$  and  $1400 \text{ cm}^{-1}$ , specifically, the peaks at  $835 \text{ cm}^{-1}$  ( $Q^1$ ),  $902 \text{ cm}^{-1}$  ( $Q^2$ ),  $977 \text{ cm}^{-1}$  ( $Q^3$ ), and  $1350 \text{ cm}^{-1}$  ( $\text{Si}-\text{O}^-$ ) are associated with asymmetric and symmetric Si–O stretching vibrations in M–S–H (Figure 2).<sup>25,26,30,35,36</sup> On the other hand, the peaks at  $1635$  and  $3383 \text{ cm}^{-1}$  are associated with H–O–H bending vibrations of molecularly bound  $\text{H}_2\text{O}$  and O–H stretching (Figure 2),<sup>4,30,37,38</sup> whereas the sharp peak at  $3692 \text{ cm}^{-1}$  is associated with brucite.<sup>37</sup>

Thermogravimetric analysis reveals weight losses in three distinct regions (Figure 3). The first region ( $20\text{--}250^\circ\text{C}$ ) is associated with poorly bound water, including monolayer, multilayer, and interlayer water within M–S–H.<sup>30,43,44</sup> This region may also include bulk water at a high relative humidity. The second weight loss in M–S–H with a Mg/Si ratio of 1 is observed between  $320$  and  $450^\circ\text{C}$  and is primarily related to the dehydroxylation of Si–OH groups (Figure 3a).<sup>25,43–46</sup> The third weight loss, occurring at  $580^\circ\text{C}$ , is associated with the dehydroxylation of Mg–OH groups.<sup>25</sup> Dehydroxylation of serpentine minerals has been observed between  $670$  and  $900^\circ\text{C}$ , whereas the inner OH groups linked to the magnesium in the talc structure dehydroxylates between  $750$  and  $1000^\circ\text{C}$ , in agreement with the weight losses observed for M–S–H from

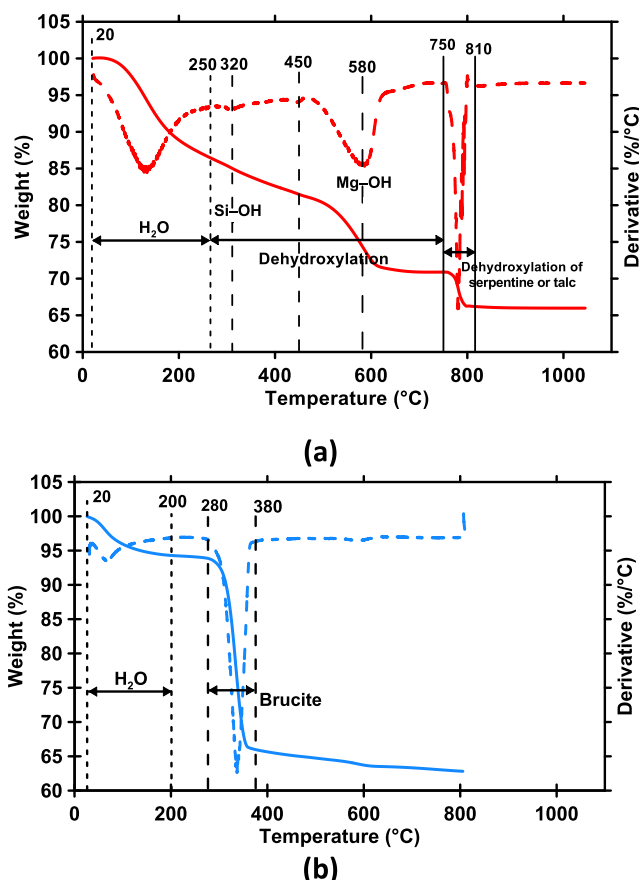


**Figure 3.** Decomposition curves of the precipitates grown from a solution containing either (a)  $[\text{Mg}] = [\text{Si}] = 100 \text{ mM}$  or (b)  $[\text{Mg}] = [\text{OH}] = 100 \text{ mM}$  for 48 h at  $25 \pm 2^\circ\text{C}$ . The derivative of the mass loss is shown by the dashed curves.

450 to  $1000^\circ\text{C}$ .<sup>47</sup> In contrast, the brucite sample shows a single distinct sharp peak in this region at around  $320^\circ\text{C}$ , which is primarily attributed to the release of hydroxylated water (Figure 3b).<sup>46</sup>

SEM-EDS analysis (Figure 4) shows that the Mg-to-Si molar ratios of the precipitates range from 0.64 to 1.02 with an average of 0.85 (Table 3), indicating the predominance of M–S–H, since previous studies have shown that the Mg/Si ratio of M–S–H precipitates closely matches that of the growth solution.<sup>29,36</sup> Taken together, the combination of analytical techniques employed herein provides evidence for the

**Table 3. Results of EDS Analysis of Precipitates Grown from a Solution Containing  $[\text{Mg}] = [\text{Si}] = 100 \text{ mM}$ , Showing the Molar % for Selected Points and Areas ( $\sim 510 \mu\text{m} \times 680 \mu\text{m}$ ) in SEM Images**

	N	O	Na	Mg	Si	Mg/Si
point 1	1.63	67.26	5.19	13.10	12.82	1.02
point 2	1.35	67.29	3.42	13.82	14.12	0.98
point 3	0.00	54.06	2.93	16.68	26.32	0.64
point 4	0.00	63.32	4.44	14.59	17.65	0.83
point 5	3.23	59.76	7.13	13.17	16.71	0.79
area 1	0.00	63.97	7.23	13.40	15.39	0.87
area 2	0.00	63.00	8.00	12.00	14.00	0.86

persistence of primarily M–S–H under our experimental conditions.

### 3.2. Influence of Morphology and Reaction Time on the Elastic Modulus of M–S–H

The conditions for the synthesis of M–S–H overgrowths on mica are shown in Table 2. The discrepancy between the calculated and initial pH is likely caused by instantaneous (within seconds) precipitation of M–S–H.<sup>4</sup>

A representative topography (amplitude modulation) image and its corresponding frequency distribution show M–S–H overgrowths that are up to  $\sim 2 \mu\text{m}$  thick on the mica (001) surface (Figure 5a). A uniform film is not obtained; instead, two types of morphologies are observed: (1) large and faceted and (2) small and irregular. The corresponding elastic modulus map and its frequency distribution are shown in Figure 5b. For the sake of clarity, frequency distributions for subset areas of the elastic modulus map are also shown (right, Figure 5b). The results reveal significant variations in elastic modulus depending on morphology; i.e., large, faceted grains feature an average elastic modulus of  $54.0 \pm 14.9 \text{ GPa}$ , whereas small, irregular grains have an average elastic modulus of  $6.0 \pm 7.0 \text{ GPa}$  (Figure 4b). As high as 75 GPa is obtained for faceted grains, indicating increased stiffness and resistance to deformation. These observations highlight the potential role of morphological control in fine-tuning the elastic modulus of M–S–H cements. For comparison, the elastic modulus of brucite has been previously reported as 11 GPa based on neutron diffraction data<sup>48</sup> and 15 GPa based on Brillouin scattering.<sup>49</sup> The elastic modulus of amorphous alkali–silica reaction gels has been measured to be between 24.9 and 34.0 GPa.<sup>50</sup> Using nanoscale three-point bending tests with an atomic force microscope, amorphous  $\text{SiO}_2$  nanowires have been found to

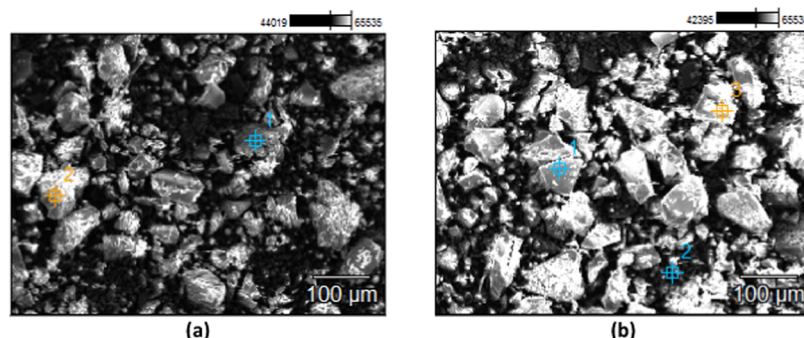


**Figure 4.** Scanning electron micrographs of the M–S–H precipitates grown from a solution containing  $[\text{Mg}] = [\text{Si}] = 100 \text{ mM}$  for 48 h at  $25 \pm 2^\circ\text{C}$ , showing corresponding micrographs where the chemical compositions for (a) Point 1, Point 2, and Area 1 and (b) Point 3, Point 4, Point 5, and Area 2 in Table 3 are collected.

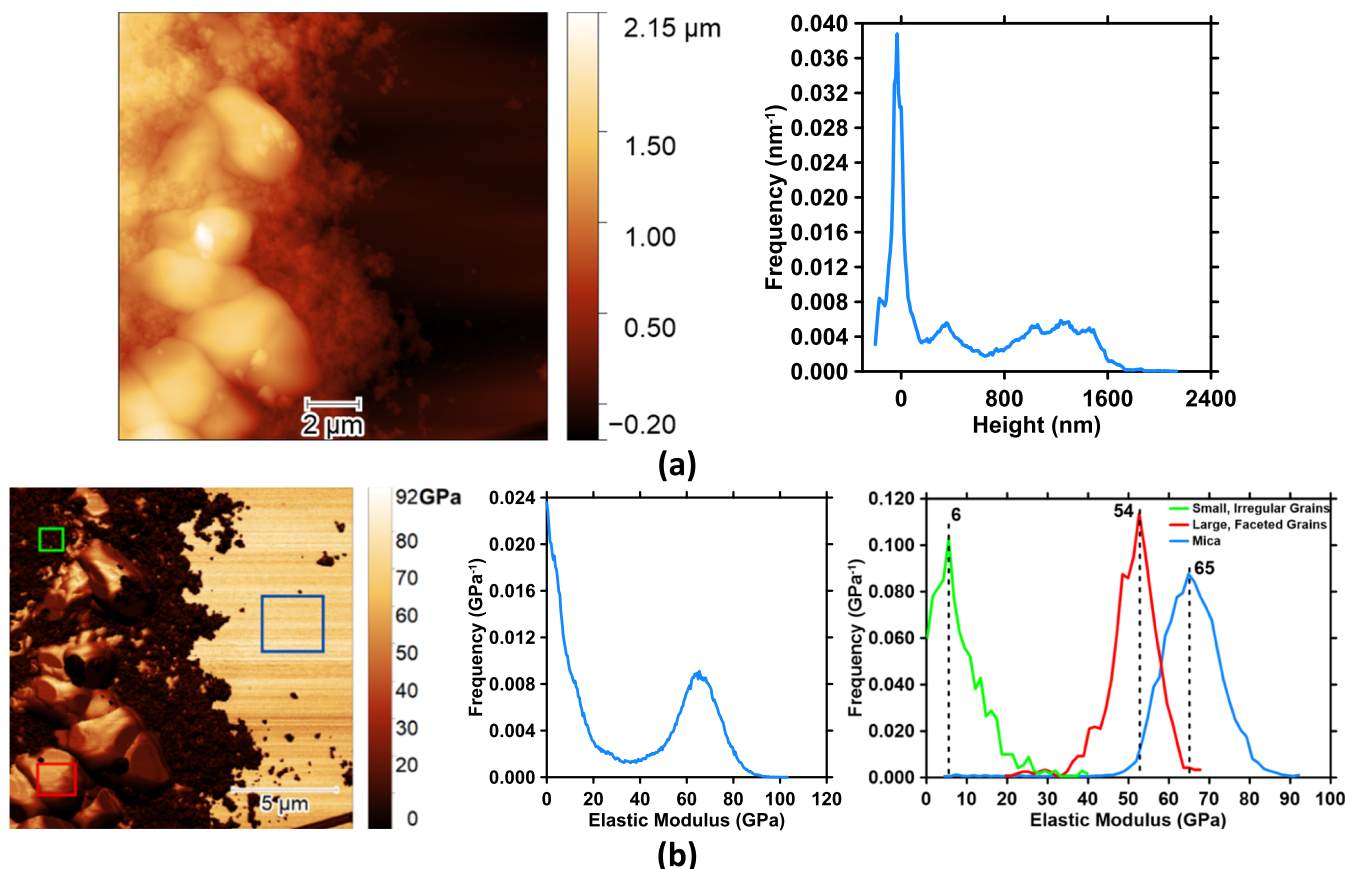


**Figure 5.** Representative atomic force microscopy images of (a, left) surface topography and (a, right) corresponding frequency distribution of height with an RMS (roughness) of 545.3 nm, and (b) elastic modulus and (b, middle and right) corresponding frequency distribution of elastic modulus of mica (001) reacted with a supersaturated solution of M–S–H with a final concentration of  $[\text{Mg}] = [\text{Si}] = 100 \text{ mM}$  for 48 h at  $24.1^\circ\text{C}$ . In panel (b, left), the frequency distribution for the entire area of panel (b, left) is shown. In panel (b, right), the frequency distributions for subset areas in panel (b, left) are shown.

have an elastic modulus of  $76.6 \pm 7.2 \text{ GPa}$ .<sup>51</sup> Additionally, the elastic modulus of silica glass, as determined using molecular dynamics simulation, is  $72.56 \text{ GPa}$ .<sup>52</sup>

Representative topography and elastic modulus data for relatively short (40 min) and long (48 h) experimental durations are shown in Figure 6. Higher spatial resolution images are listed in Figure 7. Specifically, a shorter reaction time resulted in the formation of monodisperse grains that are small and irregular, whereas a longer reaction time resulted in the occurrence of both morphology types, as shown in Figure 5. This suggests that the extended reaction time allowed for the development of precipitates with greater structural diversity. In agreement with the findings in Figure 5, early age precipitates exhibited relatively low elastic modulus values of  $10.0 \pm 7.0 \text{ GPa}$  (Figure 6a). Late-age precipitates featured a significantly higher elastic modulus value of approximately  $57.2 \pm 14.9 \text{ GPa}$  (Figure 6b,c). Elastic modulus measurements on 24 h samples (see Table 2) show a similar bimodal distribution of elastic modulus that depends on the precipitate morphology.

The tip–sample contact area, which may change as a result of surface roughness, may affect elastic modulus measurements.<sup>53</sup> Nonetheless, it is evident in Figure 6a that precipitate roughness does not result in significant differences in the elastic modulus (see Figure 7 for a detailed characterization of the morphology). On the other hand, changes in the contact area can partly or wholly explain the varying elastic modulus of faceted grains depending on the facet orientation (Figure 5b).

Despite these uncertainties, the observation of a bimodal distribution (and the respective average values) of the elastic modulus is unchanged. Furthermore, the discrepancy between local tip–sample contact areas increases with increasing indentation depth; this source of error is minimized through the use of small indentation depths in AM–FM.<sup>54</sup>

### 3.3. Effect of Silicate Polymerization on Elastic Modulus: Comparison with C–S–H and across Mg-to-Si Ratios

The elastic modulus of M–S–H is also evaluated as a function of solution  $[\text{Mg}]/[\text{Si}]$  molar ratios: 0.5, 1.0, 1.5, and 2.0. Notably, it has been shown previously that the precipitate Mg/Si ratio reasonably matches the  $[\text{Mg}]/[\text{Si}]$  of the initial growth solution.<sup>44</sup> The elastic modulus of faceted grains is invariant with the Mg/Si ratio and ranges from  $\sim 40$  to  $64 \text{ GPa}$  across different samples and areas within samples (Table 2, Figure 8). On the other hand, small, irregular grains whose elastic modulus ranged from  $\sim 5$  to  $15 \text{ GPa}$  showed a slight decrease with the Mg/Si ratio (Figure 8). The lower elastic modulus of small, irregular grains can be attributed to their lower degree of crystallinity<sup>55</sup> compared to the faceted grains.<sup>56</sup>

C–S–H has an elastic modulus that ranges between 20 and  $40 \text{ GPa}$ , as measured using nanoindentation and viscoelastic modulus mapping.<sup>57</sup> This range lies between the average values for faceted and irregular M–S–H precipitates (Figure 8). This suggests that the higher elastic modulus in faceted M–S–H grains arises from their sheet-like structure (i.e., dominance of  $\text{Q}^3$  sites) as in phyllosilicates<sup>58–61</sup> and that the lower elastic

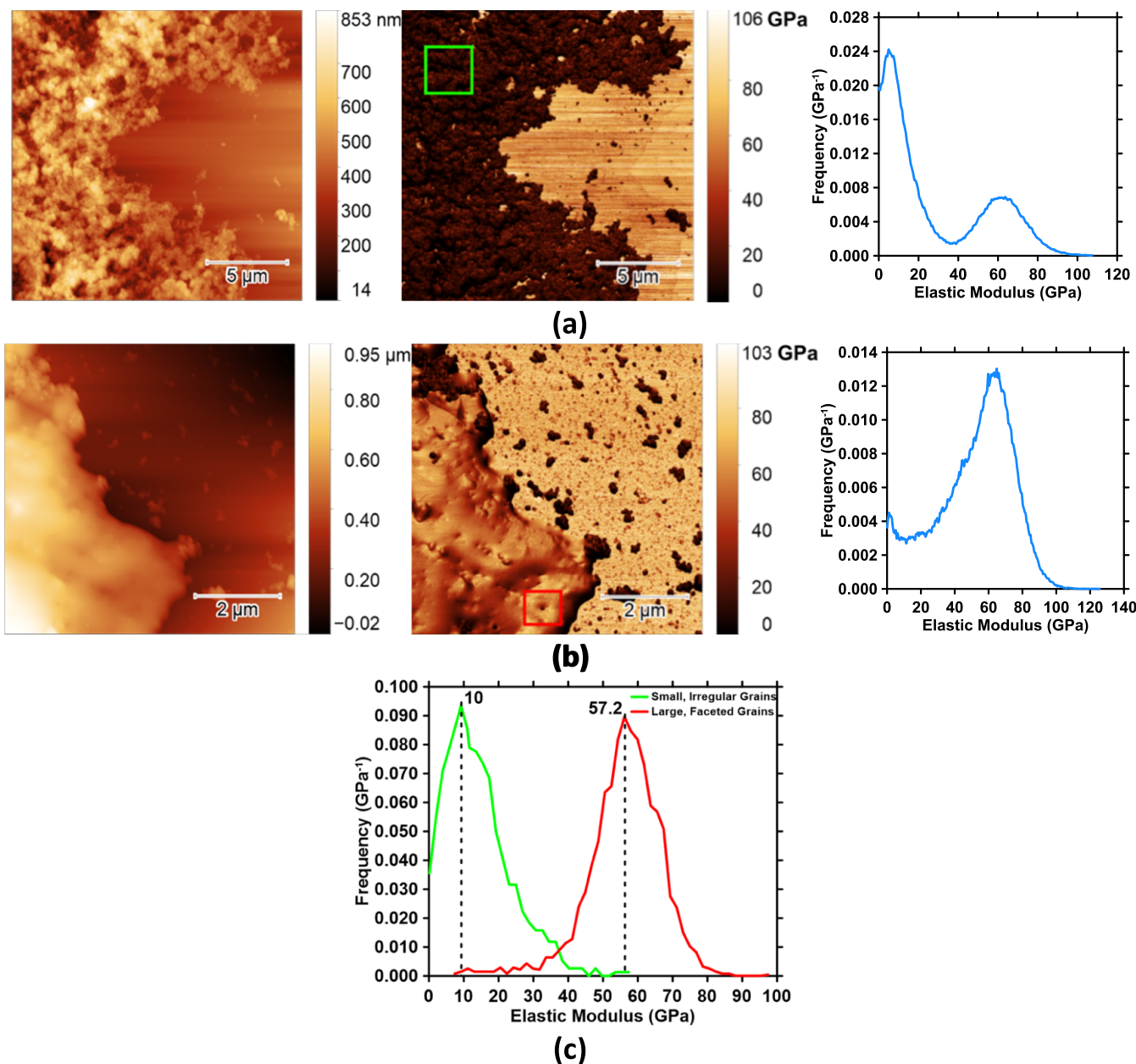


**Figure 6.** Representative atomic force microscopy maps of (left) topography and (middle) corresponding elastic modulus, and (right) frequency distribution of elastic modulus of mica (001) reacted with a supersaturated solution of M–S–H with a final concentration of  $[\text{Mg}] = [\text{Si}] = 100$  mM for (a) 40 min at 23.1 °C with an RMS (roughness) value of 100.8 nm or (b) 48 h at 24.1 °C with an RMS (roughness) value of 197.4 nm. In panel (c), the elastic modulus distributions for small, irregular grains and large, faceted grains marked by boxes in panels (a) and (b) are shown.

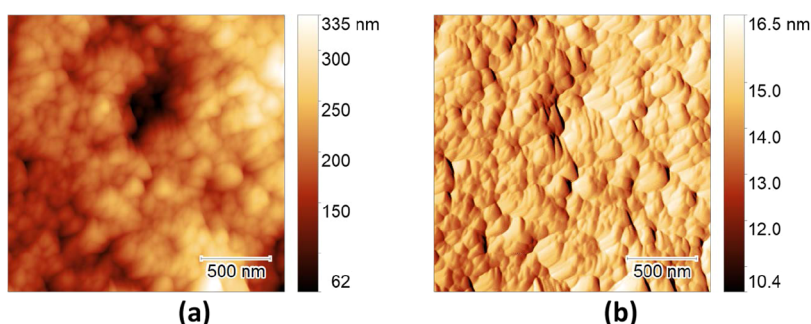


**Figure 7.** Representative atomic force microscopy (a) height and (b) amplitude error images of mica (001) reacted with a supersaturated solution of M–S–H with a final concentration of  $[\text{Mg}] = 50$  mM and  $[\text{Si}] = 100$  mM for 48.3 h, showing detail of M–S–H precipitates similar to those shown in Figure 6a.

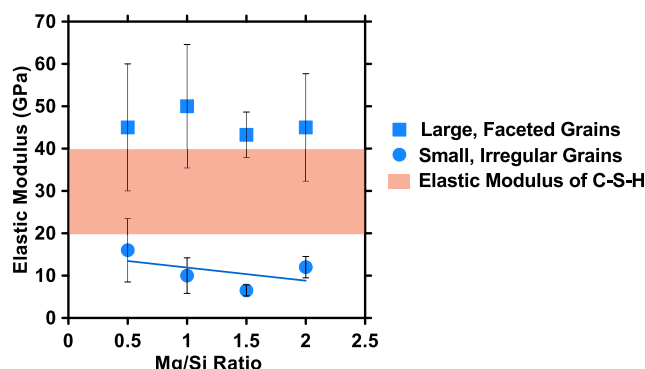


**Figure 8.** Elastic modulus of M–S–H as a function of Mg/Si ratio, given for large, faceted grains and small, irregular grains. Error bars represent the standard deviation for two repeat measurements on different areas within the same sample (i.e., 48-h samples in Table 2). The elastic modulus range for C–S–H is also shown for comparison. The RMS (roughness) values are 183.2 and 104.3 nm for Mg/Si = 0.5, 545.3 and 197.4 nm for Mg/Si = 1, 421.4 and 218.8 nm for Mg/Si = 1.5, and 89.59 and 131.7 nm for Mg/Si = 2. Therefore, the average RMS is 236.5 nm, and the standard deviation of the RMS is 162.2 nm.

modulus of C–S–H compared to M–S–H can be explained by C–S–H’s less polymerized chain-like silicate structure.<sup>62</sup>

In C–S–H, it has been shown that as the Ca/Si ratio increases, the length of the silicate chains decreases.<sup>63,64</sup> It has also been shown that Ca/Si ratios influence the relative distributions of Q<sup>2</sup> and Q<sup>1</sup> species; specifically, an increase in the Ca/Si ratio results in the relative reduction of Q<sup>2</sup> species,<sup>59</sup> suggesting a decreased degree of polymerization of silica tetrahedra.<sup>58,65</sup> We have previously shown that the degree of polymerization of M–S–H decreases with increasing Mg/Si ratio.<sup>4</sup> Therefore, we propose that the small, irregular M–S–H precipitates (e.g., Figure 6a)<sup>55</sup> may have varying degrees of polymerization that are controlled by the Mg/Si ratio. This implies that the observed reduction in elastic modulus in poorly crystalline M–S–H is analogous to that observed in C–S–H.<sup>59</sup> Significantly, in addition to the Ca/Si ratio, particle packing, porosity, and interplanar distance influence the mechanical characteristics of C–S–H.<sup>59</sup> We postulate that similar operative mechanisms can be applied to M–S–H.

#### 4. CONCLUSIONS

This study presents the first experimental measurements of the elastic modulus of the cementitious material magnesium silicate hydrate. Detailed characterization of precipitates shows that M–S–H is the primary phase that forms under the experimental conditions. Topographical imaging using AFM revealed two distinct morphological features: small, irregular grains and large, faceted grains. Simultaneous elastic modulus mapping indicates that these features have corresponding elastic modulus values of 5 to 15 GPa and 40 to 64 GPa. The elastic modulus of poorly crystalline M–S–H decreased with increasing Mg/Si ratio possibly because of a corresponding decreased degree of polymerization analogous to the behavior observed in C–S–H. This could also explain the higher elastic modulus of large, faceted M–S–H compared to that of C–S–H. The results of this study have important implications in the synthesis of cementitious materials for construction applications. Taken together, this study demonstrates that the deliberate control of the morphology and

chemical composition of M–S–H may be a viable pathway for tailoring cement properties to meet specific performance requirements.

#### AUTHOR INFORMATION

##### Corresponding Author

Erika La Plante – Department of Materials Science and Engineering, University of California, Davis, Davis, California 95616, United States; [orcid.org/0000-0002-5273-9523](https://orcid.org/0000-0002-5273-9523); Email: [elaplante@ucdavis.edu](mailto:elaplante@ucdavis.edu)

##### Authors

Arif Syed – Department of Materials Science and Engineering, University of Texas at Arlington, Arlington, Texas 76019, United States

Trinh Thao My Nguyen – Department of Materials Science and Engineering, University of California, Davis, Davis, California 95616, United States

Complete contact information is available at: <https://pubs.acs.org/10.1021/acsenm.4c00071>

#### Notes

The authors declare no competing financial interest.

#### ACKNOWLEDGMENTS

The authors acknowledge financial support provided by the National Science Foundation (NSF CAREER Award #2342381). This work is performed at the Materials Chemistry Laboratory (MCL), the Center for Advanced Construction Materials (CACM), and the Characterization Center for Materials and Biology (CCMB) at the University of Texas at Arlington. The authors also acknowledge the support that has made the operations of these laboratories possible. The contents of this paper reflect the views and opinions of the authors, who are responsible for the accuracy of the datasets presented herein, and do not reflect the views and/or policies of the agency, nor do the contents constitute a specification, standard, or regulation.

#### REFERENCES

- Gartner, E.; Gimenez, M.; Meyer, V.; Pisch, A. A Novel Atmospheric Pressure Approach to the Mineral Capture of CO<sub>2</sub> from Industrial Point Sources. In *Thirteenth Annual Conference on Carbon Capture; Utilization and Storage*; Pittsburgh, PA, 2014.
- Zhang, F. Magnesium Oxide Based Binders as Low-Carbon Cements (PhD Thesis). Imperial College London, 2012.
- Vandeperre, L. J.; Liska, M.; Al-Tabbaa, A. Hydration and Mechanical Properties of Magnesia, Pulverized Fuel Ash, and Portland Cement Blends. *J. Mater. Civ. Eng.* **2008**, *20*, 375–383.
- Singh, D.; Nguyen, T. T. M.; Bustamantes, E.; Wahab, A.; Yousaf, A. H.; Shortt, I.; Foss, F. W.; Konsta-Gdoutos, M.; Lee, S. S.; La Plante, E. Chemical Structure and Complex Growth Modes of Magnesium Silicate Hydrate: Nanoparticle Orientation, Aggregation, and Fusion. *Cem. Concr. Res.* **2024**, *175*, No. 107367.
- Mohamad, N.; Muthusamy, K.; Embong, R.; Kusbiantoro, A.; Hashim, M. H. Environmental Impact of Cement Production and Solutions: A Review. *Mater. Today: Proc.* **2022**, *48*, 741–746.
- Tyrrell, T. Calcium Carbonate Cycling in Future Oceans and Its Influence on Future Climates. *Journal of Plankton Research* **2007**, *30* (2), 141–156.
- Huntington, T. G. The Potential for Calcium Depletion in Forest Ecosystems of Southeastern United States: Review and Analysis. *Global Biogeochem. Cycles* **2000**, *14* (2), 623–638.

(8) *Soil-Calcium Depletion Linked to Acid Rain and Forest Growth in the Eastern United States*, US Geological Survey, 1999, DOI: 10.3133/wri984267.

(9) Korolev, A. S.; Kopp, A.; Odnoburcev, D.; Loskov, V.; Shimanovsky, P.; Koroleva, Y.; Vatin, N. I. Compressive and Tensile Elastic Properties of Concrete: Empirical Factors in Span Reinforced Structures Design. *Materials* **2021**, *14* (24), 7578.

(10) Jiang, W.; Yuan, D.; Zhang, S.; Bao, R.; Xiao, J.; Wu, W.; Wang, T. Experimental Analysis of Deformation-Adapted Binders and Their Mixture Performance. *Constr. Build. Mater.* **2023**, *389*, No. 131733.

(11) Li, P.; Zhang, Y.; Duan, S.; Huang, R.; Gu, J. Variation Pattern of the Elastic Modulus of Concrete under Combined Humidity and Heat Conditions. *Materials* **2023**, *16* (15), 5447.

(12) Helal, J.; Sofi, M.; Mendis, P. Non-Destructive Testing of Concrete: A Review of Methods. *Electron. J. Struct. Eng.* **2015**, *14*, 97–105.

(13) Velez, K.; Maximilien, S.; Damidot, D.; Fantozzi, G.; Sorrentino, F. Determination by Nanoindentation of Elastic Modulus and Hardness of Pure Constituents of Portland Cement Clinker. *Cem. Concr. Res.* **2001**, *31* (4), 555–561.

(14) Gönder, H. Y.; Demirel, M. G.; Mohammadi, R.; Alkurt, S.; Fidancioğlu, Y. D.; Yüksel, I. B. The Effects of Using Cements of Different Thicknesses and Amalgam Restorations with Different Young's Modulus Values on Stress on Dental Tissue: An Investigation Using Finite Element Analysis. *Coatings* **2023**, *13* (1), 6.

(15) Hajilar, S.; Shafei, B. Nano-Scale Investigation of Elastic Properties of Hydrated Cement Paste Constituents Using Molecular Dynamics Simulations. *Comput. Mater. Sci.* **2015**, *101*, 216–226.

(16) Kocab, D.; Kucharczykova, B.; Misak, P.; Zitt, P.; Kralikova, M. Development of the Elastic Modulus of Concrete under Different Curing Conditions. *Procedia Eng.* **2017**, *195*, 96–101.

(17) Nguyen, T.-T.; Thai, H.-T.; Ngo, T. Optimised Mix Design and Elastic Modulus Prediction of Ultra-High Strength Concrete. *Constr. Build. Mater.* **2021**, *302*, No. 124150.

(18) Khatri, R. P.; Sirivivatnanon, V.; Gross, W. Effect of Different Supplementary Cementitious Materials on Mechanical Properties of High Performance Concrete. *Cem. Concr. Res.* **1995**, *25* (1), 209–220.

(19) Proksch, R. Multifrequency, Repulsive-Mode Amplitude-Modulated Atomic Force Microscopy. *Appl. Phys. Lett.* **2006**, *89*, No. 113121.

(20) Benaglia, S.; Amo, C. A.; Garcia, R. Fast, Quantitative and High Resolution Mapping of Viscoelastic Properties with Bimodal AFM. *Nanoscale* **2019**, *11*, 15289.

(21) AM-FM Viscoelastic Mapping Mode ©; Oxford Instruments Asylum Research Inc.

(22) Escalante-García, J.; Sharp, J. H. The Microstructure and Mechanical Properties of Blended Cements Hydrated at Various Temperatures. *Cem. Concr. Res.* **2001**, *31* (5), 695–702.

(23) Kjellsen, K. O.; Detwiler, R. J.; Gjørv, O. E. Pore Structure of Plain Cement Pastes Hydrated at Different Temperatures. *Cem. Concr. Res.* **1990**, *20* (6), 927–933.

(24) Ben Haha, M.; Le Saout, G.; Winnefeld, F.; Lothenbach, B. Influence of Activator Type on Hydration Kinetics, Hydrate Assemblage and Microstructural Development of Alkali Activated Blast-Furnace Slags. *Cem. Concr. Res.* **2011**, *41* (3), 301–310.

(25) Bernard, E.; Lothenbach, B.; Chlique, C.; Wyrzykowski, M.; Dauzères, A.; Pochard, I.; Cau-Dit-Coumes, C. Characterization of Magnesium Silicate Hydrate (M-S-H). *Cem. Concr. Res.* **2019**, *116*, 309–330.

(26) Nied, D.; Enemark-Rasmussen, K.; L'Hopital, E.; Skibsted, J.; Lothenbach, B. Properties of Magnesium Silicate Hydrates (M-S-H). *Cem. Concr. Res.* **2016**, *79*, 323–332.

(27) Brew, D. R. M.; Glasser, F. P. Synthesis and Characterisation of Magnesium Silicate Hydrate Gels. *Cem. Concr. Res.* **2005**, *35*, 85–98.

(28) Zhang, T.; Vandeperre, L. J.; Cheeseman, C. R. Development of Magnesium Silicate Hydrate Cement System for Nuclear Waste Encapsulation; NUWCEM: Avignon, 2011; pp 582–591.

(29) Simoni, M.; Woo, C. L.; Zhao, H.; Iuga, D.; Svora, P.; Hanein, T.; Kinoshita, H.; Walkley, B. Reaction Mechanisms, Kinetics, and Nanostructural Evolution of Magnesium Silicate Hydrate (M-S-H) Gels. *Cem. Concr. Res.* **2023**, *174*, No. 107295.

(30) Zhang, Y.; Li, Y.; Xu, Y.; Sang, S.; Jin, S. Enhanced Formation of Magnesium Silica Hydrates (M-S-H) Using Sodium Metasilicate and Caustic Magnesia in Magnesia Castables. *Ceram. Int.* **2017**, *43* (12), 9110–9116.

(31) Frost, R. L.; Kloprogge, J. T. Infrared Emission Spectroscopic Study of Brucite. *Spectrochim. Acta, Part A* **1999**, *55*, 2195–2205.

(32) Lothenbach, B.; Nied, D.; L'Hopital, E.; Achiedo, G.; Dauzères, A. Magnesium and Calcium Silicate Hydrates. *Cem. Concr. Res.* **2015**, *77*, 60–68.

(33) Marsiske, M. R.; Debus, C.; Di Lorenzo, F.; Bernard, E.; Churakov, S. V.; Ruiz-Agudo, C. Immobilization of (Aqueous) Cations in Low pH M-S-H Cement. *Appl. Sci.* **2021**, *11*, 2968.

(34) Bernard, E.; Lothenbach, B.; Rentsch, D.; Pochard, I.; Dauzères, A. Formation of Magnesium Silicate Hydrates (M-S-H). *Phys. Chem. Earth Parts A/B/C* **2017**, *99*, 142–157.

(35) Miller, F. A.; Wilkins, C. H. Infrared Spectra and Characteristic Frequencies of Inorganic Ions. *Anal. Chem.* **1952**, *24*, 1253–1294.

(36) Brew, D. R. M.; Glasser, F. P. Synthesis and Characterisation of Magnesium Silicate Hydrate Gels. *Cem. Concr. Res.* **2005**, *35* (1), 85–98.

(37) Nied, D.; Kasper, E. R.; Emilie, L.; et al. Properties of Magnesium Silicate Hydrates (M-S-H). *Cem. Concr. Res.* **2016**, *79*, 323–332.

(38) Zhang, T.; Vandeperre, L. J.; Cheeseman, C. R. Formation of Magnesium Silicate Hydrate (M-S-H) Cement Pastes Using Sodium Hexametaphosphate. *Cem. Concr. Res.* **2014**, *65*, 8–14.

(39) Parkhurst, D. L.; Appelo, C. A. J. Description of Input and Examples for PHREEQC Version 3: a Computer Program for Speciation, Batch-Reaction, One-Dimensional Transport, and Inverse Geochemical Calculations. *Techniques and Methods*, US Geological Survey, 2013, pp 497.

(40) Lothenbach, B.; Kulik, D. A.; Matschei, T.; Balonis, M.; Baquerizo, L.; Dilnesa, B.; Miron, G. D.; Myers, R. J. Cemdata18: A Chemical Thermodynamic Database for Hydrated Portland Cements and Alkali-Activated Materials. *Cem. Concr. Res.* **2019**, *115*, 472–506.

(41) Pang, H.; Ning, G.; Gong, W.; Ye, J.; Lin, Y. Direct Synthesis of Hexagonal Mg(OH)<sub>2</sub> Nanoplates from Natural Brucite without Dissolution Procedure. *Chem. Commun.* **2011**, *47* (22), 6317.

(42) Matos, C. R. S.; Xavier, M. J.; Barreto, L. S.; Costa, N. B.; Gimenez, I. F. Principal Component Analysis of X-Ray Diffraction Patterns To Yield Morphological Classification of Brucite Particles. *Anal. Chem.* **2007**, *79* (5), 2091–2095.

(43) Li, Z.; Zhang, T.; Hu, J.; Tang, Y.; Niu, Y.; Wei, J.; Yu, Q. Characterization of Reaction Products and Reaction Process of MgO–SiO<sub>2</sub>–H<sub>2</sub>O System at Room Temperature. *Constr. Build. Mater.* **2014**, *61*, 252.

(44) Nied, D.; Enemark-Rasmussen, K.; L'Hopital, E.; Skibsted, J.; Lothenbach, B. Properties of Magnesium Silicate Hydrates (MSH). *Cem. Concr. Res.* **2016**, *79*, 323–332.

(45) Roosz, C.; Grangeon, S.; Blanc, P.; Montouillout, V.; Lothenbach, B.; Henocq, P.; Giffaut, E.; Vieillard, P.; Gaboreau, S. Crystal Structure of Magnesium Silicate Hydrates (MSH): The Relation with 2:1 Mg–Si Phyllosilicates. *Cem. Concr. Res.* **2015**, *73*, 228–237.

(46) Jin, F.; Al-Tabbaa, A. Thermogravimetric Study on the Hydration of Reactive Magnesia and Silica Mixture at Room Temperature. *Thermochim. Acta* **2013**, *566*, 162–168.

(47) Dumas, A.; Martin, F.; Le Roux, C.; Micoud, P.; Petit, S.; Ferrage, E.; Brendlé, J.; Grauby, O.; Greenhill-Hooper, M. Phyllosilicates synthesis: a way of accessing edges contributions in NMR and FTIR spectroscopies. Example of synthetic talc. *Phys. Chem. Miner.* **2013**, *40*, 361–373.

(48) Catti, M.; Ferraris, G.; Hull, S.; Pavese, A. Static Compression and H Disorder in Brucite, Mg(OH)<sub>2</sub>, to 11 GPa: A Powder Neutron Diffraction Study. *Phys. Chem. Miner.* **1995**, *22* (3), 200–206, DOI: 10.1007/BF00202300.

(49) Jiang, F.; Speziale, S.; Duffy, T. S. Single-Crystal Elasticity of Brucite,  $\text{Mg(OH)}_2$ , to 15 GPa by Brillouin Scattering. *Am. Miner.* **2006**, *91* (11–12), 1893–1900.

(50) Moon, J.; Speziale, S.; Meral, C.; Kalkan, B.; Clark, S. M.; Monteiro, P. J. M. Determination of the Elastic Properties of Amorphous Materials: Case Study of Alkali–Silica Reaction Gel. *Cem. Concr. Res.* **2013**, *54*, 55–60.

(51) Ni, H.; Li, X.; Gao, H. Elastic Modulus of Amorphous  $\text{SiO}_2$  Nanowires. *Appl. Phys. Lett.* **2006**, *88* (4), No. 043108.

(52) Liu, Q.; Lu, Z.; Zhu, M.; Yuan, Z.; Yang, Z.; Hu, Z.; Li, J. Simulation of the Tensile Properties of Silica Aerogels: The Effects of Cluster Structure and Primary Particle Size. *Soft Matter* **2014**, *10* (33), 6266–6277.

(53) Labuda, A.; Kocun, M.; Meinhold, W.; Walters, D.; Proksch, R. Generalized Hertz Model for Bimodal Nanomechanical Mapping. *Beilstein J. Nanotechnol.* **2016**, *7*, 970–982.

(54) Benaglia, S.; Amo, C. A.; Garcia, R. Fast, Quantitative and High Resolution Mapping of Viscoelastic Properties with Bimodal AFM. *Nanoscale* **2019**, *11* (32), 15289–15297.

(55) Moshiri, A.; Stefaniuk, D.; Smith, S. K.; Morshedifard, A.; Rodrigues, D. F.; Qomi, M. J. A.; Krakowiak, K. J. Structure and Morphology of Calcium-Silicate-Hydrates Cross-Linked with Dipodal Organosilanes. *Cem. Concr. Res.* **2020**, *133*, No. 106076.

(56) Doroudiani, S.; Park, C. B.; Kortschot, M. T. Effect of the Crystallinity and Morphology on the Microcellular Foam Structure of Semicrystalline Polymers. *Polym. Eng. Sci.* **1996**, *36* (21), 2645–2662.

(57) Xu, J.; Corr, D. J.; Shah, S. P. Nanomechanical Properties of C-S-H Gel/Cement Grain Interface by Using Nanoindentation and Modulus Mapping. *J. Zhejiang Univ., Sci. A* **2015**, *16* (1), 38–46.

(58) Maddalena, R. Synthesis of Calcium Silicate Hydrate (C-S-H) and Novel Cementitious Materials: Characterisation, Engineering Applications and Environmental Aspects Doctoral thesis, 2018 DOI: [10.48730/h41y-r875](https://doi.org/10.48730/h41y-r875).

(59) Pelisser, F.; Gleize, P. J. P.; Mikowski, A. Effect of the Ca/Si Molar Ratio on the Micro/Nanomechanical Properties of Synthetic C-S-H Measured by Nanoindentation. *J. Phys. Chem. C* **2012**, *116* (32), 17219–17227.

(60) Humbert, S.; Lame, O.; Séguéla, R.; Vigier, G. A Re-Examination of the Elastic Modulus Dependence on Crystallinity in Semi-Crystalline Polymers. *Polymer* **2011**, *52* (21), 4899–4909.

(61) Mileva, D.; Zia, Q.; Androsch, R. Tensile Properties of Random Copolymers of Propylene with Ethylene and 1-Butene: Effect of Crystallinity and Crystal Habit. *Polym. Bull.* **2010**, *65* (6), 623–634.

(62) Liu, L.; Sun, C.; Geng, G.; Feng, P.; Li, J.; Dähn, R. Influence of Decalcification on Structural and Mechanical Properties of Synthetic Calcium Silicate Hydrate (C-S-H). *Cem. Concr. Res.* **2019**, *123*, No. 105793.

(63) Richardson, I. G. The Calcium Silicate Hydrates. *Cem. Concr. Res.* **2008**, *38* (2), 137–158.

(64) Ioannidou, K.; Krakowiak, K. J.; Bauchy, M.; Hoover, C. G.; Masoero, E.; Yip, S.; Ulm, F.-J.; Levitz, P.; Pellenq, R. J.-M.; Del Gado, E. Mesoscale Texture of Cement Hydrates. *Proc. Natl. Acad. Sci. U.S.A.* **2016**, *113* (8), 2029–2034.

(65) Alizadeh, R. A. Nanostructure and Engineering Properties of Basic and Modified Calcium-Silicate-Hydrate Systems. Doctoral dissertation, University of Ottawa: Canada, 2009 DOI: [10.13140/RG.2.1.3892.8089](https://doi.org/10.13140/RG.2.1.3892.8089).